

Elucidating the Exposure Bias in Diffusion Models

Mang Ning¹, Mingxiao Li², Jianlin Su³, Albert Ali Salah¹, Itir Onal Ertugrul¹

¹Utrecht University

²KU Leuven

³Moonshot AI Ltd.

m.ning@uu.nl, mingxiao.li@cs.kuleuven.be, bojone@spaces.ac.cn, a.a.salah@uu.nl, i.onalertugrul@uu.nl

Abstract

Diffusion models have demonstrated impressive generative capabilities, but their ‘exposure bias’ problem, described as the input mismatch between training and sampling, lacks in-depth exploration. In this paper, we systematically investigate the exposure bias problem in diffusion models by first analytically modelling the sampling distribution, based on which we then attribute the prediction error at each sampling step as the root cause of the exposure bias issue. Furthermore, we discuss potential solutions to this issue and propose an intuitive metric for it. Along with the elucidation of exposure bias, we propose a simple, yet effective, training-free method called Epsilon Scaling to alleviate the exposure bias. We show that Epsilon Scaling explicitly moves the sampling trajectory closer to the vector field learned in the training phase by scaling down the network output (Epsilon), mitigating the input mismatch between training and sampling. Experiments on various diffusion frameworks (ADM, DDPM/DDIM, LDM), unconditional and conditional settings, and deterministic vs. stochastic sampling verify the effectiveness of our method.

Introduction

Due to the outstanding generation quality and diversity, diffusion models (Sohl-Dickstein et al. 2015; Ho, Jain, and Abbeel 2020; Song and Ermon 2019) have achieved unprecedented success in image generation (Dhariwal and Nichol 2021; Nichol et al. 2022; Rombach et al. 2022; Saharia et al. 2022), audio synthesis (Kong et al. 2021; Chen et al. 2021) and video generation (Ho et al. 2022). Unlike generative adversarial networks (GANs) (Goodfellow et al. 2014), variational autoencoders (VAEs) (Kingma and Welling 2014) and flow-based models (Dinh, Krueger, and Bengio 2014; Dinh, Sohl-Dickstein, and Bengio 2017), diffusion models stably learn the data distribution through a noise/score prediction objective and progressively removes noise from random initial vectors in the iterative sampling stage.

A key feature of diffusion models is that good sample quality requires a long iterative sampling chain since the Gaussian assumption of reverse diffusion only holds for small step sizes (Xiao et al. 2022). However, Ning et al. (2023) claim that the iterative sampling chain also leads to the *exposure bias* problem (Ranzato et al. 2016; Schmidt

2019). Concretely, given the noise prediction network $\epsilon_{\theta}(\cdot)$, exposure bias refers to the input mismatch between training and inference, where the former is always exposed to the ground truth training sample \mathbf{x}_t while the latter depends on the previously generated sample $\hat{\mathbf{x}}_t$. The difference between \mathbf{x}_t and $\hat{\mathbf{x}}_t$ causes the discrepancy between $\epsilon_{\theta}(\mathbf{x}_t)$ and $\epsilon_{\theta}(\hat{\mathbf{x}}_t)$, which leads to the error accumulation and the sampling drift (Li et al. 2023a).

We point out that the exposure bias problem in diffusion models lacks in-depth exploration. For example, there is no proper metric to quantify the exposure bias and no explicit error analysis for it. To shed light on exposure bias, we conduct a systematical investigation in this paper by first modelling the sampling distribution with prediction error. Based on our analysis, we find that the practical sampling distribution has a variance larger than the ground truth distribution at every single step, demonstrating the analytic difference between \mathbf{x}_t in training and $\hat{\mathbf{x}}_t$ in sampling. Along with the sampling distribution analysis, we propose a metric δ_t to evaluate exposure bias by comparing the variance difference between training and sampling. Finally, we discuss potential solutions to exposure bias, and propose a simple yet effective *training-free and plug-in* method called Epsilon Scaling to alleviate this issue.

We test our approach on three different diffusion frameworks using deterministic and stochastic sampling, and on conditional and unconditional generation tasks. Without affecting the recall and precision (Kynkäänniemi et al. 2019), our method yields dramatic Fréchet Inception Distance (FID) improvements. For instance, with 20-step sampling, Epsilon Scaling achieves a FID 4.31 on the CIFAR-10 dataset, outperforming the baseline FID 10.36 by a large margin. Also, we illustrate that Epsilon Scaling effectively reduces the exposure bias by moving the sampling trajectory towards the training trajectory.

Overall, our contributions in this paper are:

- We systematically investigate the exposure bias problem in diffusion models and define a metric for it.
- We suggest potential solutions to the exposure bias issue and propose a training-free, plug-in method (Epsilon Scaling) which significantly improves the sample quality.
- Our extensive experiments demonstrate the generality of Epsilon Scaling and it can be widely applied to different

diffusion architectures and applications.

Related Work

Diffusion models were introduced by Sohl-Dickstein et al. (2015) and later improved by Song and Ermon (2019), Ho et al. (2020) and Nichol et al. (2021). Song et al. (2021) unify score-based models and Denoising Diffusion Probabilistic Models (DDPMs) via stochastic differential equations. Furthermore, Karras et al. (2022) disentangle the design space of diffusion models and introduce the EDM model to further boost the performance in image generation. With the advances in diffusion theory, conditional generation (Ho et al. 2022, Choi et al. 2021) also flourishes in various scenarios, including text-to-image generation (Nichol et al. 2022; Ramesh et al. 2022; Rombach et al. 2022; Saharia et al. 2022), controllable image synthesis (Zhang and Agrawala 2023; Li et al. 2023b; Zheng et al. 2023), as well as generating other modalities, for instance, audio (Chen et al. 2021; Kong et al. 2021), object shape (Zhou et al. 2021) and time series (Rasul et al. 2021). In the meantime, accelerating the time-consuming reverse diffusion sampling has been extensively investigated in many works (Song, Meng, and Ermon 2021; Lu et al. 2022; Liu et al. 2022). For example, distillation (Salimans and Ho 2022), Restart sampler (Xu et al. 2023) and fast ODE samplers (Zhao et al. 2023) have been proposed to speed up the sampling.

The phenomenon of exposure bias within the diffusion model was first identified by Ning et al. (2023). They introduced an extra noise at each step during the training to mitigate the discrepancy between training and inference, thereby reducing the impact of exposure bias. Additionally, another approach presented by (Li et al. 2023a) sought to address exposure bias without necessitating retraining of the model. Their method involved a manipulation of the time step during the backward generation process. However, the exposure bias in diffusion models still lacks illuminating research in terms of the explicit sampling distribution, metric and root cause, which is the objective of this paper. Besides, we propose a solution called Epsilon Scaling in the sampling phase based on the observation of the prediction deviation between training and sampling. This method, while straightforward, proves effective in mitigating the exposure bias issue.

Exposure Bias in Diffusion Models

Background

We first briefly review the formulation of DDPMs from Ho et al. (2020). Given a sample \mathbf{x}_0 from the data distribution $q(\mathbf{x}_0)$ and a well-behaved noise schedule $(\beta_1, \dots, \beta_T)$, DDPM defines the forward process as a Markov chain and iteratively adds Gaussian noise until obtaining a pure noise image $\mathbf{x}_T \sim \mathcal{N}(\mathbf{0}, \mathbf{I})$:

$$q(\mathbf{x}_{1:T}|\mathbf{x}_0) = \prod_{t=1}^T q(\mathbf{x}_t|\mathbf{x}_{t-1}) \quad (1)$$

$$q(\mathbf{x}_t|\mathbf{x}_{t-1}) = \mathcal{N}(\mathbf{x}_t; \sqrt{1 - \beta_t}\mathbf{x}_{t-1}, \beta_t\mathbf{I}) \quad (2)$$

A notable property of the Gaussian forward process defined in Eq. 2 is that it allows us to sample \mathbf{x}_t directly conditioned on the input \mathbf{x}_0 :

$$q(\mathbf{x}_t|\mathbf{x}_0) = \mathcal{N}(\mathbf{x}_t; \sqrt{\bar{\alpha}_t}\mathbf{x}_0, (1 - \bar{\alpha}_t)\mathbf{I}), \quad (3)$$

$$\mathbf{x}_t = \sqrt{\bar{\alpha}_t}\mathbf{x}_0 + \sqrt{1 - \bar{\alpha}_t}\boldsymbol{\epsilon}, \quad (4)$$

where $\bar{\alpha}_t = \prod_{i=1}^t \alpha_i$, $\alpha_t = 1 - \beta_t$ and $\boldsymbol{\epsilon} \sim \mathcal{N}(\mathbf{0}, \mathbf{I})$. Then, the reverse distribution $q(\mathbf{x}_{t-1}|\mathbf{x}_t)$ is approximated by a neural network (parameterised by $\boldsymbol{\theta}$), from which we can sample $\mathbf{x}_T \sim \mathcal{N}(\mathbf{0}, \mathbf{I})$ and iteratively run the following reverse process to get a sample from $q(\mathbf{x}_0)$:

$$p_{\boldsymbol{\theta}}(\mathbf{x}_{t-1}|\mathbf{x}_t) = \mathcal{N}(\mathbf{x}_{t-1}; \boldsymbol{\mu}_{\boldsymbol{\theta}}(\mathbf{x}_t, t), \sigma_t\mathbf{I}) \quad (5)$$

The optimisation objective of $p_{\boldsymbol{\theta}}(\mathbf{x}_{t-1}|\mathbf{x}_t)$ is derived from the variational lower bound (VLB) of the log-likelihood $p_{\boldsymbol{\theta}}(\mathbf{x}_0)$ and is further simplified as the Kullback–Leibler divergence:

$$L_{t-1} = D_{KL}(q(\mathbf{x}_{t-1}|\mathbf{x}_t, \mathbf{x}_0) || p_{\boldsymbol{\theta}}(\mathbf{x}_{t-1}|\mathbf{x}_t)), \quad (6)$$

in which the ground truth forward process posterior $q(\mathbf{x}_{t-1}|\mathbf{x}_t, \mathbf{x}_0)$ is tractable when conditioned on \mathbf{x}_0 using Bayes theorem:

$$q(\mathbf{x}_{t-1}|\mathbf{x}_t, \mathbf{x}_0) = \mathcal{N}(\mathbf{x}_{t-1}; \tilde{\boldsymbol{\mu}}(\mathbf{x}_t, \mathbf{x}_0), \tilde{\beta}_t\mathbf{I}) \quad (7)$$

$$\tilde{\boldsymbol{\mu}}(\mathbf{x}_t, \mathbf{x}_0) = \frac{\sqrt{\bar{\alpha}_{t-1}}\beta_t}{1 - \bar{\alpha}_t}\mathbf{x}_0 + \frac{\sqrt{\alpha_t}(1 - \bar{\alpha}_{t-1})}{1 - \bar{\alpha}_t}\mathbf{x}_t \quad (8)$$

$$\tilde{\beta}_t = \frac{1 - \bar{\alpha}_{t-1}}{1 - \bar{\alpha}_t}\beta_t \quad (9)$$

Given Eq. 8 and Eq. 4, Ho et al (2020) found that parameterising $\boldsymbol{\mu}_{\boldsymbol{\theta}}(\mathbf{x}_t, t)$ with a neural network predicting $\boldsymbol{\epsilon}$ worked the best in practice:

$$\boldsymbol{\mu}_{\boldsymbol{\theta}}(\mathbf{x}_t, t) = \frac{\sqrt{\bar{\alpha}_{t-1}}\beta_t}{1 - \bar{\alpha}_t}\boldsymbol{x}_{\boldsymbol{\theta}}(\mathbf{x}_t, t) + \frac{\sqrt{\alpha_t}(1 - \bar{\alpha}_{t-1})}{1 - \bar{\alpha}_t}\mathbf{x}_t \quad (10)$$

$$= \frac{1}{\sqrt{\alpha_t}}\left(\mathbf{x}_t - \frac{\beta_t}{\sqrt{1 - \bar{\alpha}_t}}\boldsymbol{\epsilon}_{\boldsymbol{\theta}}(\mathbf{x}_t, t)\right), \quad (11)$$

where $\boldsymbol{x}_{\boldsymbol{\theta}}(\mathbf{x}_t, t)$ denotes the denoising model which predicts \mathbf{x}_0 given \mathbf{x}_t and $\boldsymbol{x}_{\boldsymbol{\theta}}(\mathbf{x}_t, t)$ practically is replaced by $\frac{\mathbf{x}_t - \sqrt{1 - \bar{\alpha}_t}\boldsymbol{\epsilon}_{\boldsymbol{\theta}}(\mathbf{x}_t, t)}{\sqrt{\alpha_t}}$ according to Eq. 4 in the above derivation.

For simplicity, we use $\mathbf{x}_{\boldsymbol{\theta}}^t$ as the short notation of $\boldsymbol{x}_{\boldsymbol{\theta}}(\mathbf{x}_t, t)$ in the rest of this paper.

Finally, $\boldsymbol{\epsilon}_{\boldsymbol{\theta}}(\cdot)$ is trained with the simplified loss function:

$$L(\boldsymbol{\theta}) = \mathbb{E}_{\mathbf{x}_0, \boldsymbol{\epsilon}, t} [||\boldsymbol{\epsilon} - \boldsymbol{\epsilon}_{\boldsymbol{\theta}}(\mathbf{x}_t, t)||^2]. \quad (12)$$

Sampling Distribution with Prediction Error

The exposure bias problem of diffusion models is described as the input mismatch between \mathbf{x}_t during training and $\hat{\mathbf{x}}_t$ during sampling (Ning et al. 2023). In this section, we explicitly derive the sampling distribution $q(\hat{\mathbf{x}}_t|\mathbf{x}_{t+1}, \mathbf{x}_{\boldsymbol{\theta}}^{t+1})$ and compare it with the training distribution $q(\mathbf{x}_t|\mathbf{x}_0)$, where the former shows the $\hat{\mathbf{x}}_t$ seen by the network in the sampling phase, while the latter is the \mathbf{x}_t seen by the network during training.

Comparing Eq. 8 with Eq. 10, Xiao et al. (2022) note that the sampling distribution $p_{\boldsymbol{\theta}}(\mathbf{x}_{t-1}|\mathbf{x}_t)$ is in fact parameterised as:

$$p_{\boldsymbol{\theta}}(\mathbf{x}_{t-1}|\mathbf{x}_t) = q(\mathbf{x}_{t-1}|\mathbf{x}_t, \mathbf{x}_{\boldsymbol{\theta}}^t) \quad (13)$$

where \mathbf{x}_θ^t means the predicted \mathbf{x}_0 given \mathbf{x}_t . Therefore, the practical sampling paradigm is that we first predict ϵ using $\epsilon_\theta(\mathbf{x}_t, t)$. Then we derive the estimation \mathbf{x}_θ^t for \mathbf{x}_0 using Eq. 4. Finally based on the ground truth posterior $q(\mathbf{x}_{t-1}|\mathbf{x}_t, \mathbf{x}_0)$, \mathbf{x}_{t-1} is generated using $q(\mathbf{x}_{t-1}|\mathbf{x}_t, \mathbf{x}_\theta^t)$ by replacing \mathbf{x}_0 with \mathbf{x}_θ^t . Since $q(\mathbf{x}_{t-1}|\mathbf{x}_t, \mathbf{x}_\theta^t) = q(\mathbf{x}_{t-1}|\mathbf{x}_t, \mathbf{x}_0)$ holds only if $\mathbf{x}_\theta^t = \mathbf{x}_0$, this requires the network to make no prediction error about \mathbf{x}_0 to ensure $q(\mathbf{x}_{t-1}|\mathbf{x}_t, \mathbf{x}_\theta^t)$ share the same variance with $q(\mathbf{x}_{t-1}|\mathbf{x}_t, \mathbf{x}_0)$. However, $\mathbf{x}_\theta^t - \mathbf{x}_0$ is practically non-zero and we claim that the prediction error of \mathbf{x}_0 needs to be considered to derive the real sampling distribution. Following Analytic-DPM (Bao et al. 2022b) and Bao et al. (2022a), we model \mathbf{x}_θ^t as $p_\theta(\mathbf{x}_0|\mathbf{x}_t)$ and approximate it by a Gaussian distribution:

$$p_\theta(\mathbf{x}_0|\mathbf{x}_t) = \mathcal{N}(\mathbf{x}_\theta^t; \mathbf{x}_0, e_t^2 \mathbf{I}) \quad (14)$$

$$\mathbf{x}_\theta^t = \mathbf{x}_0 + e_t \epsilon_0 \quad (15)$$

where e_t is the standard deviation of \mathbf{x}_θ^t and $\epsilon_0 \sim \mathcal{N}(\mathbf{0}, \mathbf{I})$.

Taking the prediction error into account, we now compute the sampling distribution $q(\hat{\mathbf{x}}_t|\mathbf{x}_{t+1}, \mathbf{x}_\theta^{t+1})$ which is the same distribution as $q(\mathbf{x}_{t-1}|\mathbf{x}_t, \mathbf{x}_\theta^t)$ by substituting with the index $t+1$ and using $\hat{\mathbf{x}}_t$ to highlight it is generated in the sampling stage. Based on Eq. 7, we know

$$q(\hat{\mathbf{x}}_t|\mathbf{x}_{t+1}, \mathbf{x}_\theta^{t+1}) = \mathcal{N}(\hat{\mathbf{x}}_t; \mu_\theta(\mathbf{x}_{t+1}, t+1), \tilde{\beta}_{t+1} \mathbf{I}) \quad (16)$$

Its mean and variance can be further derived according to Eq. 10 and Eq. 9, respectively. Thus, a sample $\hat{\mathbf{x}}_t$ is:

$$\begin{aligned} \hat{\mathbf{x}}_t &= \mu_\theta(\mathbf{x}_{t+1}, t+1) + \sqrt{\tilde{\beta}_{t+1}} \epsilon_1 \\ &= \frac{\sqrt{\tilde{\alpha}_t} \beta_{t+1}}{1 - \tilde{\alpha}_{t+1}} \mathbf{x}_\theta^{t+1} + \frac{\sqrt{\alpha_{t+1}}(1 - \tilde{\alpha}_t)}{1 - \tilde{\alpha}_{t+1}} \mathbf{x}_{t+1} + \sqrt{\tilde{\beta}_{t+1}} \epsilon_1 \end{aligned} \quad (17)$$

Plugging Eq. 15 and Eq. 4 (using index $t+1$) into Eq. 17, we obtain the final analytical form of $\hat{\mathbf{x}}_t$ (see Appendix for the full derivation):

$$\hat{\mathbf{x}}_t = \sqrt{\tilde{\alpha}_t} \mathbf{x}_0 + \sqrt{1 - \tilde{\alpha}_t + \left(\frac{\sqrt{\tilde{\alpha}_t} \beta_{t+1}}{1 - \tilde{\alpha}_{t+1}} e_{t+1}\right)^2} \epsilon_3 \quad (18)$$

in which, $\epsilon_1, \epsilon_2, \epsilon_3 \sim \mathcal{N}(\mathbf{0}, \mathbf{I})$. From Eq. 18, we can derive the mean and variance of $q(\hat{\mathbf{x}}_t|\mathbf{x}_{t+1}, \mathbf{x}_\theta^{t+1})$ and compare them with the parameters of $q(\mathbf{x}_t|\mathbf{x}_0)$. In Table 1, $q(\mathbf{x}_t|\mathbf{x}_0)$ shows the \mathbf{x}_t seen by the network during training while $q(\hat{\mathbf{x}}_t|\mathbf{x}_{t+1}, \mathbf{x}_\theta^{t+1})$ indicates the $\hat{\mathbf{x}}_t$ exposed to the network during sampling.

Table 1: The mean and variance of $q(\mathbf{x}_t|\mathbf{x}_0)$ during training and $q(\hat{\mathbf{x}}_t|\mathbf{x}_{t+1}, \mathbf{x}_\theta^{t+1})$ during sampling.

	Mean	Variance
$q(\mathbf{x}_t \mathbf{x}_0)$	$\sqrt{\tilde{\alpha}_t} \mathbf{x}_0$	$(1 - \tilde{\alpha}_t) \mathbf{I}$
$q(\hat{\mathbf{x}}_t \mathbf{x}_{t+1}, \mathbf{x}_\theta^{t+1})$	$\sqrt{\tilde{\alpha}_t} \mathbf{x}_0$	$(1 - \tilde{\alpha}_t + \left(\frac{\sqrt{\tilde{\alpha}_t} \beta_{t+1}}{1 - \tilde{\alpha}_{t+1}} e_{t+1}\right)^2) \mathbf{I}$

Exposure Bias Due to Prediction Error

It is clear from Table 1 that the variance of the sampling distribution $q(\hat{\mathbf{x}}_t|\mathbf{x}_{t+1}, \mathbf{x}_\theta^{t+1})$ is always larger than the variance of the training distribution $q(\mathbf{x}_t|\mathbf{x}_0)$ by the magnitude $\left(\frac{\sqrt{\tilde{\alpha}_t} \beta_{t+1}}{1 - \tilde{\alpha}_{t+1}} e_{t+1}\right)^2$. Note that, this variance gap between training and sampling is produced just in a single reverse diffusion step given that the network $\epsilon_\theta(\cdot)$ can get access to the ground truth input \mathbf{x}_{t+1} . What makes the situation even worse is that the error of single-step sampling will be accumulated in the multi-step regressive sampling, resulting in an explosion of sampling variance error.

On CIFAR-10 dataset (Krizhevsky et al. 2009), we designed an experiment to statistically measure both the single-step variance error and multi-step variance error of $q(\hat{\mathbf{x}}_t|\mathbf{x}_{t+1}, \mathbf{x}_\theta^{t+1})$ using 20 steps sampling (see Appendix for the experimental details). The results in Fig. 1 indicate that the closer to $t=0$, the larger the variance error of multi-step sampling. The explosion of sampling variance error results in the sampling drift (exposure bias) problem and we attribute the prediction error $\mathbf{x}_\theta^t - \mathbf{x}_0$ as the root cause of the exposure bias in diffusion models.

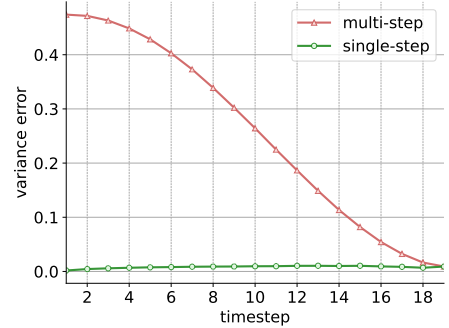


Figure 1: Variance error of the sampling distribution in single-step sampling and multi-step sampling.

Intuitively, a possible solution to exposure bias is using a sampling noise variance β' , which is smaller than $\tilde{\beta}_t$, to counteract the extra variance term $\left(\frac{\sqrt{\tilde{\alpha}_t} \beta_{t+1}}{1 - \tilde{\alpha}_{t+1}} e_{t+1}\right)^2$ caused by the prediction error $\mathbf{x}_\theta^t - \mathbf{x}_0$. Unfortunately, $\tilde{\beta}_t$ is the lower bound of the sampling noise schedule $\tilde{\beta}_t \in [\tilde{\beta}_t, \beta_t]$, where the lower bound and upper bound are the sampling variances given by $q(\mathbf{x}_0)$ being a delta function and isotropic Gaussian function, respectively (Nichol and Dhariwal 2021). Therefore, we can draw a conclusion that the exposure bias problem can not be alleviated by manipulating the sampling noise schedule $\tilde{\beta}_t$.

Interestingly, Bao et al. (2022b) analytically provide the optimal sampling noise schedule β_t^* which is larger than the lower bound $\tilde{\beta}_t$. Based on what we discussed earlier, a larger noise schedule β_t^* would cause a more severe exposure bias issue. A strange phenomenon, but not explained by the authors, in Bao et al. (2022b) is that β_t^* leads to a worse sample quality (FID) than using $\tilde{\beta}_t$ under 1000 sampling steps. We believe the exposure bias is in the position to account for this

phenomenon: under the long sampling, the negative impact of exposure bias exceeds the positive gain of the optimal variance β_t^* .

Metric for Exposure Bias

Although some literature has already discussed the exposure bias problem in diffusion models (Ning et al. 2023; Li et al. 2023a), there still lacks a well-defined and straightforward metric for this concept. Since we have shown in Section that the exposure bias issue can be represented as the sampling drift, we thus propose to use the variance error of the sampling distribution $q(\hat{\mathbf{x}}_t | \mathbf{x}_{t+1}, \mathbf{x}_\theta^{t+1})$ to quantify the exposure bias. In order to ensure that our metric reflect the sampling drift for the real sampling process, we measure the variance error in the regular consecutive sampling process. Thereby, our metric δ_t for exposure bias is defined as:

$$\delta_t = \hat{\beta}_t - \bar{\beta}_t \quad (19)$$

where $\bar{\beta}_t = 1 - \bar{\alpha}_t$ denotes the variance of $q(\mathbf{x}_t | \mathbf{x}_0)$ during training and $\hat{\beta}_t$ presents the variance of $q(\hat{\mathbf{x}}_t | \mathbf{x}_{t+1}, \mathbf{x}_\theta^{t+1})$ in the consecutive sampling process which starts from \mathbf{x}_T . Our method of measuring δ_t is described in Algorithm 1.

Algorithm 1: Measurement of Exposure Bias δ_t

```

1: Initialize  $\delta_t = 0, n_t = list() (\forall t \in \{1, \dots, T - 1\})$ 
2: repeat
3:    $\mathbf{x}_0 \sim q(\mathbf{x}_0), \boldsymbol{\epsilon} \sim \mathcal{N}(\mathbf{0}, \mathbf{I})$ 
4:   compute  $\mathbf{x}_T$  using Eq. 4
5:   for  $t := T, \dots, 1$  do
6:     if  $t == T$  then  $\hat{\mathbf{x}}_t = \mathbf{x}_T$ 
7:      $\hat{\mathbf{x}}_{t-1} = \frac{1}{\sqrt{\alpha_t}}(\hat{\mathbf{x}}_t - \frac{\beta_t}{\sqrt{1-\alpha_t}}\boldsymbol{\epsilon}_\theta(\hat{\mathbf{x}}_t, t)) + \sqrt{\hat{\beta}_t}\mathbf{z}$  ( $\mathbf{z} \sim \mathcal{N}(\mathbf{0}, \mathbf{I})$ )
8:      $n_{t-1}.append(\hat{\mathbf{x}}_{t-1} - \sqrt{\bar{\alpha}_{t-1}}\mathbf{x}_0)$ 
9:   end for
10: until  $N$  iterations
11: for  $t := T, \dots, 1$  do
12:    $\hat{\beta}_t = \text{numpy.var}(n_t)$ 
13:    $\delta_t = \hat{\beta}_t - \bar{\beta}_t$ 
14: end for

```

The key step of Algorithm 1 is that we subtract the mean $\sqrt{\bar{\alpha}_{t-1}}\mathbf{x}_0$ and the remaining term $\hat{\mathbf{x}}_{t-1} - \sqrt{\bar{\alpha}_{t-1}}\mathbf{x}_0$ corresponds to the stochastic term of $q(\hat{\mathbf{x}}_{t-1} | \mathbf{x}_t, \mathbf{x}_\theta^t)$. In our experiments, we use $N = 50,000$ samples to compute the variance $\hat{\beta}_t$.

Solution Discussion

We now discuss possible solutions to the exposure bias issue of diffusion models based on the analysis throughout Section . We highlight that the prediction error of $\mathbf{x}_\theta^t - \mathbf{x}_0$ is the root cause of exposure bias. Thus, the most straightforward way of reducing exposure bias is learning an accurate $\boldsymbol{\epsilon}$ or score function (Song and Ermon 2019) prediction network. For example, by delicately designing the network and hyper-parameter tuning, EDM (Karras et al. 2022) improves

the FID from 3.01 to 2.51 on CIFAR-10 dataset, presenting significant improvement.

Secondly, we believe that data augmentation can reduce the risk of learning inaccurate $\boldsymbol{\epsilon}$ or score function for $\hat{\mathbf{x}}_t$ by learning a denser vector field than vanilla diffusion models. For instance, Karras et al. (2022) has shown that the geometric augmentation (Karras et al. 2020) benefits the network training and sample quality. In the same spirit, DDPM-IP (Ning et al. 2023) augment each training sample \mathbf{x}_t by a Gaussian term and receive substantial improvements in FID.

However, it is worth pointing out that the above-mentioned methods require retraining the network and expensive parameter searching during the training. This naturally drives us to the question: *can we alleviate the exposure bias in the sampling stage without any retraining?*

Method

Epsilon Scaling

In Section , we have concluded that the exposure bias issue can not be solved by reducing the sampling noise variance, thus another direction to be explored in the sampling phase is the prediction of the network $\boldsymbol{\epsilon}_\theta(\cdot)$. Since we already know from Table 1 that \mathbf{x}_t inputted to the network $\boldsymbol{\epsilon}_\theta(\cdot)$ in training differs from $\hat{\mathbf{x}}_t$ fed into the network $\boldsymbol{\epsilon}_\theta(\cdot)$ in sampling, we are interested in the question that what is the difference in the output of $\boldsymbol{\epsilon}_\theta(\cdot)$ between training and inference?

For simplicity, we denote the output of $\boldsymbol{\epsilon}_\theta(\cdot)$ as $\boldsymbol{\epsilon}_\theta^t$ in training and as $\boldsymbol{\epsilon}_\theta^s$ in sampling. Although the ground truth of $\boldsymbol{\epsilon}_\theta^s$ is not accessible during inference, we are still able to speculate the behaviour of $\boldsymbol{\epsilon}_\theta^s$ from an L2-norm perspective. In Fig. 2, we plot the L2-norm of $\boldsymbol{\epsilon}_\theta^t$ and $\boldsymbol{\epsilon}_\theta^s$ at each sampling step. In detail, $\boldsymbol{\epsilon}_\theta^t$ is collected in a single step sampling given a well-trained model and the ground truth input \mathbf{x}_t , i.e. $\boldsymbol{\epsilon}_\theta^t = \boldsymbol{\epsilon}_\theta(\mathbf{x}_t, t)$. In contrast, $\boldsymbol{\epsilon}_\theta^s$ is gathered in the real consecutive sampling process, namely $\boldsymbol{\epsilon}_\theta^s = \boldsymbol{\epsilon}_\theta(\hat{\mathbf{x}}_t, t)$. It is clear from Fig. 2 that the L2-norm of $\boldsymbol{\epsilon}_\theta^s$ is always larger than that of $\boldsymbol{\epsilon}_\theta^t$, implying a biased prediction network $\boldsymbol{\epsilon}_\theta(\hat{\mathbf{x}}_t, t)$ during inference. In other words, the network $\boldsymbol{\epsilon}_\theta(\cdot)$ learns an inaccurate vector field $\boldsymbol{\epsilon}_\theta^s$ around each $(\hat{\mathbf{x}}_t, t)$ with the vector length longer than that of $\boldsymbol{\epsilon}_\theta^t$.

One can infer that the prediction $\boldsymbol{\epsilon}_\theta^s$ could be improved if we can move the input $(\hat{\mathbf{x}}_t, t)$ from the inaccurate vector field (green curve in Fig. 3) towards the reliable vector field (red curve in Fig. 3). To this end, we propose to scale down $\boldsymbol{\epsilon}_\theta^s$ by a factor λ_t at sampling timestep t . Our solution is based on the observation: $\boldsymbol{\epsilon}_\theta^t$ and $\boldsymbol{\epsilon}_\theta^s$ share the same input $\mathbf{x}_T \sim \mathcal{N}(\mathbf{0}, \mathbf{I})$ at timestep $t = T$, but from timestep $T - 1$, $\hat{\mathbf{x}}_t$ (input of $\boldsymbol{\epsilon}_\theta^s$) starts to diverge from \mathbf{x}_t (input of $\boldsymbol{\epsilon}_\theta^t$) due to the biased prediction $\boldsymbol{\epsilon}_\theta(\cdot)$ made at previous timestep. This iterative process continues along the sampling chain and results in exposure bias. Therefore, we can push $\hat{\mathbf{x}}_t$ closer to \mathbf{x}_t by scaling down the over-predicted magnitude of $\boldsymbol{\epsilon}_\theta^s$.

According to the regular sampling (Eq. 11), our sampling method only differs in the λ_t term and is expressed as:

$$\mu_\theta(\mathbf{x}_t, t) = \frac{1}{\sqrt{\alpha_t}}\left(\mathbf{x}_t - \frac{\beta_t}{\sqrt{1-\alpha_t}} \frac{\boldsymbol{\epsilon}_\theta(\mathbf{x}_t, t)}{\lambda_t}\right) \quad (20)$$

Note that, our Epsilon Scaling adds no computational load

to the original sampling of diffusion models, serving as a plug-in method with zero cost.

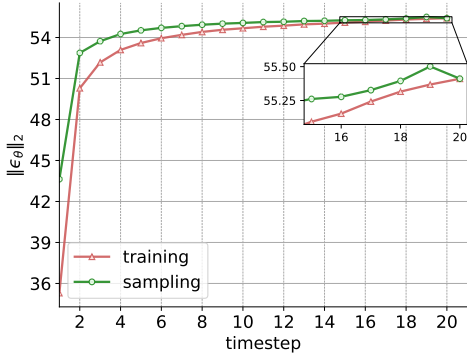


Figure 2: The L2-norm of $\epsilon_{\theta}(\cdot)$ during training and sampling on CIFAR-10. We use 20 steps sampling and report the statistical L2-norm of ϵ_{θ}^s and ϵ_{θ}^t using 50k samples at each timestep t .

The Design of Scaling Schedule

Intuitively, the scaling schedule λ_t should be directly decided by the L2-norm quotient $\frac{\|\epsilon_{\theta}^s\|_2}{\|\epsilon_{\theta}^t\|_2}$, denoted as $\Delta N(t)$, at each timestep t . However, we emphasise that $\Delta N(t)$ reflects the accumulated effect of the biased prediction error made at each timestep $T, T-1, \dots, t$. Suppose the L2-norm of ϵ_{θ}^t to be scaled at timestep t is λ_t , then $\Delta N(t)$ satisfy:

$$\Delta N(t) = \int_t^T \lambda_t dt \quad (21)$$

given a linearly distributed vector field learned by $\epsilon_{\theta}(\cdot)$ in the vicinity of \mathbf{x}_t : $\|\hat{\mathbf{x}}_t - \mathbf{x}_t\|_2 = c(\|\epsilon_{\theta}(\hat{\mathbf{x}}_t)\|_2 - \|\epsilon_{\theta}(\mathbf{x}_t)\|_2)$, where c is a constant. In practice, $\Delta N(t) \approx \int_t^T \lambda_t dt$ holds for a non-overfitting network $\epsilon_{\theta}(\cdot)$.

As shown by Nichol and Dhariwal (2021) and Benny and Wolf (2022), the $\epsilon_{\theta}(\cdot)$ predictions near $t = 0$ are very bad with the loss larger than other timesteps by several orders of magnitude. Thereby, we can ignore the area close to $t = 0$ to design λ_t , because scaling a problematic $\epsilon_{\theta}(\cdot)$ does not lead to a better predicted ϵ . We plot the $\Delta N(t)$ curve in the cases of 20 steps and 50 steps sampling in Fig. 3. It shows that $\Delta N(t)$ can be fitted by a quadratic function in the interval $t \sim (5, T)$. As a result, the integrand λ_t is a linear function:

$$\lambda_t = kt + b \quad (22)$$

where k, b are constants. Another observation from Fig. 3 is that $\Delta N(t)$ under 50-step sampling has a smaller curvature than 20-step sampling. This tendency applies to a larger sampling step, for example, 100-step sampling presents a flatter curvature than 50-step sampling in our experiments. Overall, the design principle for λ_t is that the longer the sampling step, the smaller k we should use. In Section , we will see that k is practically a small number and would decay to 0 around 50 sampling steps.

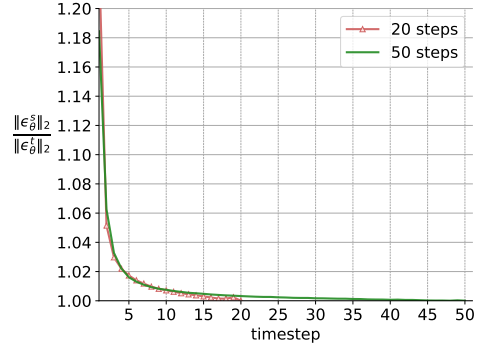


Figure 3: L2-norm quotient $\frac{\|\epsilon_{\theta}^s\|_2}{\|\epsilon_{\theta}^t\|_2}$ at timestep t under 20 and 50 steps sampling.

Results

In this section, we evaluate the performance of the proposed Epsilon Scaling method on different datasets using FID (Heusel et al. 2017). To demonstrate that Epsilon Scaling is a generic solution to exposure bias, we test the approach on various diffusion frameworks: ADM, DDPM/DDIM and LDM under stochastic and deterministic samplings, for both conditional and unconditional settings. Following the fast sampling paradigm in the diffusion community (Karras et al. 2022), we apply the sampling steps T' less than the training diffusion step T and we focus on $T' \leq 100$ for practical usages. Our FID computation is consistent with (Dhariwal and Nichol 2021) for equal comparison. All FIDs are reported using 50k generated samples and the full training set as the reference batch, except for the LSUN dataset where we follow (Dhariwal and Nichol 2021) and use 50k training samples as the reference batch. Lastly, Epsilon Scaling does not affect the precision and recall, and we report these results in Appendix .

Main Results on ADM

Since Epsilon Scaling is a training-free method, we utilise the pre-trained ADM model as the baseline and compare it against our ADM-ES (ADM with Epsilon Scaling) on datasets CIFAR-10 (Krizhevsky et al. 2009), LSUN tower (Yu et al. 2015) and FFHQ (karras et al. 2019) for unconditional generation and on datasets ImageNet 64×64 and ImageNet 128×128 (Chrabaszcz et al. 2017) for class-conditional generation. We employ the resampling technique (Nichol and Dhariwal 2021) to enable fast stochastic sampling.

Table 2 shows that independently of the dataset and the number of sampling steps T' , our ADM-ES outperforms ADM by a large margin in terms of FID, indicating the remarkable effectiveness of Epsilon Scaling. For instance, on FFHQ 128×128 , ADM-ES exhibits less than half the FID of ADM with 7.75, 16.65 and 34.52 FID improvement under 100, 50 and 20 sampling steps, respectively. Also, we compare Epsilon Scaling with the recent exposure bias solution called Input Perturbation (ADM-IP) which introduces a training regularization (Ning et al. 2023). We see from Ta-

Table 2: FID on ADM baseline. We compare ADM against our ADM-ES (uniform λ_t) and ADM-ES* (linear λ_t) on the left side. For the conditional generation, ImageNet 64×64 results are reported without classifier guidance and ImageNet 128×128 is under classifier guidance with scale=0.5. We also compare ADM-ES with ADM-IP (Ning et al. 2023) on the right side.

T'	Model	Unconditional			Conditional		T'	Model	Unconditional CIFAR-10 32×32
		CIFAR-10 32×32	LSUN 64×64	FFHQ 128×128	ImageNet 64×64	ImageNet 128×128			
100	ADM	3.37	3.59	14.52	2.71	3.55	100	ADM-IP (Ning et al. 2023)	2.38
	ADM-ES (ours)	2.17	2.91	6.77	2.39	3.37		ADM-ES (ours)	2.17
50	ADM	4.43	7.28	26.15	3.75	5.15	50	ADM-IP	2.91
	ADM-ES	2.49	3.68	9.50	3.07	4.33		ADM-ES	2.49
20	ADM	10.36	23.92	59.35	10.96	12.48	20	ADM-IP	6.96
	ADM-ES	5.15	8.22	26.14	7.52	9.95		ADM-ES	5.15
	ADM-ES*	4.31	7.60	24.83	7.37	9.86		ADM-ES*	4.31

ble 2 that ADM-ES is better than ADM-IP in FID with the extra advantage of no network re-training.

Note that, ADM-ES refers to the uniform schedule $\lambda_t = b$ and ADM-ES* applies the linear schedule $\lambda_t = kt + b$ in Table 2. In our experiments, we found that the slope k is approaching 0 as the sampling step T' increases. Taking CIFAR-10 as an example, ADM-ES* gains 0.84 FID improvement over ADM-ES at 20-step sampling with $k = 0.0005$. By contrast, using 50-step sampling, the optimal $k = 0.00007$ of ADM-ES* yields only 0.02 FID improvement (not shown in Table 2) compared with ADM-ES. Given this fact, we suggest a uniform schedule λ_t for practical application and the easy searching of the parameter b . We present the full parameters k, b used in all experiments in Appendix and provide detailed guidance on the choice of k, b . Overall, λ_t is around 1.005 on ADM baseline and a smaller λ_t should be used when a larger T' is chosen.

Epsilon Scaling Alleviates Exposure Bias

Apart from the FID improvements, we now show the exposure bias alleviated by our method using the proposed metric δ_t and we also demonstrate the sampling trajectory corrected by Epsilon Scaling. Using Algorithm 1, We measure δ_t on the dataset CIFAR-10 under 20-step regular sampling for ADM and ADM-ES models. Fig. 4 shows that ADM-ES obtains a lower δ_t at the end of sampling $t = 0$ than the baseline ADM, exhibiting a smaller variance error and sampling drift (see Appendix for other dataset results). Note that Epsilon Scaling might over-push the sampling trajectory away from the original one at the beginning of the sampling, which causes a harmless slightly larger δ_t .

Based on Fig. 2, we apply the same method to measure the L2-norm of $\epsilon_\theta(\cdot)$ in the sampling phase with Epsilon Scaling. Fig. 5 indicates that our method explicitly moves the original sampling trajectory to the vicinity of the vector field learned in the training phase given the condition that the $\|\epsilon_\theta(\mathbf{x}_t)\|_2$ is locally monotonic around \mathbf{x}_t . This condition is satisfied in denoising networks (Goodfellow, Bengio, and Courville 2016; Song and Ermon 2019) because of the monotonic score vectors around the local maximal probability density.

We emphasise that Epsilon Scaling corrects the magnitude error of $\epsilon_\theta(\cdot)$, but not the direction error. Thus we can not completely eliminate the exposure bias to achieve $\delta_t = 0$ or push the sampling trajectory to the exact training vector field.

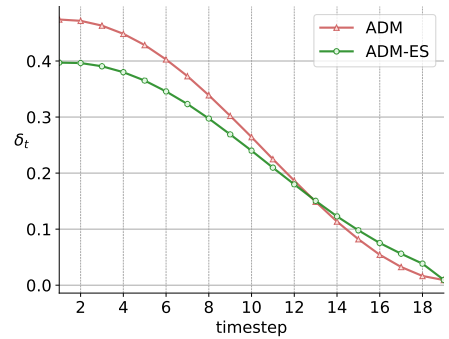


Figure 4: Exposure bias measured by δ_t . Epsilon Scaling achieves a smaller δ_t at the end of sampling ($t = 1$)

Results on DDIM/DDPM

To show the generalizability of our proposed method, we have conducted experiments encompassing the DDIM/DDPM configurations across both the CIFAR-10 and CelebA 64×64 datasets (Liu et al. 2015). The results are detailed in Table 3, wherein the designations $\eta = 0$ and $\eta = 1$ correspond to DDIM and DDPM samplers, respectively. The findings in Table 3 illustrate that our method can further boost the performance of both DDIM and DDPM samplers on the CIFAR-10 and CelebA datasets. Specifically, our proposed Epsilon Scaling technique improves the performance of DDPM sampler on CelebA dataset by 47.7%, 63.1%, 60.7% with 20, 50, and 100 sampling steps, respectively. Similar performance improvement can also be observed on CIFAR-10 dataset. We also notice that our method brings less performance improvement for DDIM sampler. This could arise from the FID advantage of deterministic sampling under a short sampling chain and the noise term in

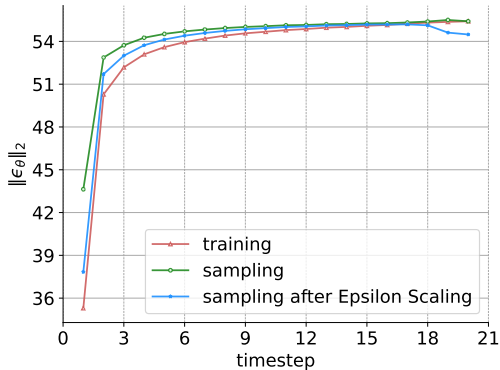


Figure 5: The L2-norm of $\epsilon_{\theta}(\cdot)$ on CIFAR-10. After applying Epsilon Scaling, the sampling $\|\epsilon_{\theta}\|_2$ (blue) gets closer to the training $\|\epsilon_{\theta}\|_2$ (red).

DDPM sampler can actively correct for errors made in earlier sampling steps, which is also discussed in Karras et al. (2022).

Table 3: FID on DDIM baseline for unconditional generations.

T'	Model	CIFAR-10 32×32		CelebA 64×64	
		$\eta = 0$	$\eta = 1$	$\eta = 0$	$\eta = 1$
100	DDIM	4.06	6.73	5.67	11.33
	DDIM-ES (ours)	3.38	4.01	5.05	4.45
50	DDIM	4.82	10.29	6.88	15.09
	DDIM-ES	4.17	4.57	6.20	5.57
20	DDIM	8.21	20.15	10.43	22.61
	DDIM-ES	6.54	7.78	10.38	11.83

Results on LDM

To further verify the generality of Epsilon Scaling, we adopt Latent Diffusion Model (LDM) as the base model which introduces an Autoencoder and performs the diffusion process in the latent space (Rombach et al. 2022). We test the performance of Epsilon Scaling (LDM-ES) on FFHQ 256×256 and CelebA-HQ 256×256 datasets using T' steps DDPM sampler.

It is clear from Table 4 that Epsilon Scaling gains substantial FID improvements on the two high-resolution datasets, where LDM-ES achieves 15.68 FID under $T' = 20$ on CelebA-HQ, almost half that of LDM. Epsilon Scaling also yields better FID under 50 and 100 sampling steps on CelebA-HQ with 7.36 FID at $T' = 100$. Similar FID improvements are obtained on FFHQ dataset over different T' .

Qualitative Comparison

In order to visually show the effect of Epsilon Scaling on image synthesis, we set the same random seed for the base

Table 4: FID on LDM baseline for unconditional generations using DDPM sampling.

T'	Model	FFHQ 256×256	CelebA-HQ 256×256
		100	LDM LDM-ES (ours)
50	LDM LDM-ES	14.34 11.57	13.95 9.16
	LDM LDM-ES	33.13 20.91	29.62 15.68

model and our Epsilon Scaling model in the sampling phase to ensure a similar trajectory for both models. Fig. 6 displays the generated samples using 100 steps on FFHQ 128×128 dataset. It is clear that ADM-ES effectively refines the sample issues of ADM, including overexposure, underexposure, coarse background and detail defects from left to right in Fig. 6 (see Appendix for more qualitative comparisons).

Besides, the qualitative comparison also empirically confirms that Epsilon Scaling guides the sampling trajectory of the base model to an adjacent but better trajectory because both models reach the same or similar modes given the common starting point x_T and the same random seed at each sampling step.



Figure 6: Qualitative comparison between ADM (first row) and ADM-ES (second row) on FFHQ 128×128

Conclusion

In this paper, we elucidate the exposure bias issue in diffusion models by analytically showing the difference between the training distribution and sampling distribution. Moreover, we discuss solutions to exposure bias and propose a training-free method to refine the deficient sampling trajectory by explicitly scaling the prediction vector. Through extensive experiments, we demonstrate that Epsilon Scaling is a generic solution to exposure bias and its simplicity enables a wide range of applications. Finally, the significant FID improvement in our method indicates the benefits of generation quality by solving the exposure bias problem. The training of an accurate Epsilon/score network is a promising direction for future research.

References

- Bao, F.; Li, C.; Sun, J.; Zhu, J.; and Zhang, B. 2022a. Estimating the Optimal Covariance with Imperfect Mean in Diffusion Probabilistic Models. In *ICML*, 1555–1584. PMLR.
- Bao, F.; Li, C.; Zhu, J.; and Zhang, B. 2022b. Analytic-dpm: an analytic estimate of the optimal reverse variance in diffusion probabilistic models. *ICLR*.
- Benny, Y.; and Wolf, L. 2022. Dynamic dual-output diffusion models. In *CVPR*, 11482–11491.
- Chen, N.; Zhang, Y.; Zen, H.; Weiss, R. J.; Norouzi, M.; and Chan, W. 2021. Wavegrad: Estimating gradients for waveform generation. *ICLR*.
- Choi, J.; Kim, S.; Jeong, Y.; Gwon, Y.; and Yoon, S. 2021. ILVR: Conditioning Method for Denoising Diffusion Probabilistic Models. In *ICCV*, 14367–14376.
- Chrabaszcz, P.; Loshchilov, I.; and Hutter, F. 2017. A down-sampled variant of imagenet as an alternative to the cifar datasets. *arXiv:1707.08819*.
- Dhariwal, P.; and Nichol, A. 2021. Diffusion models beat gans on image synthesis. *NeurIPS*, 34: 8780–8794.
- Dinh, L.; Krueger, D.; and Bengio, Y. 2014. Nice: Non-linear independent components estimation. *arXiv preprint arXiv:1410.8516*.
- Dinh, L.; Sohl-Dickstein, J.; and Bengio, S. 2017. Density estimation using real nvp. *ICLR*.
- Goodfellow, I.; Bengio, Y.; and Courville, A. 2016. *Deep Learning*. MIT Press. <http://www.deeplearningbook.org>.
- Goodfellow, I.; Pouget-Abadie, J.; Mirza, M.; Xu, B.; Warde-Farley, D.; Ozair, S.; Courville, A.; and Bengio, Y. 2014. Generative adversarial nets. *NeurIPS*, 27.
- Heusel, M.; Ramsauer, H.; Unterthiner, T.; Nessler, B.; and Hochreiter, S. 2017. Gans trained by a two time-scale update rule converge to a local nash equilibrium. *NeurIPS*, 30.
- Ho, J.; Chan, W.; Saharia, C.; Whang, J.; Gao, R.; Gritsenko, A.; Kingma, D. P.; Poole, B.; Norouzi, M.; Fleet, D. J.; et al. 2022. Imagen video: High definition video generation with diffusion models. *arXiv preprint arXiv:2210.02303*.
- Ho, J.; Jain, A.; and Abbeel, P. 2020. Denoising diffusion probabilistic models. *NeurIPS*, 33: 6840–6851.
- Ho, J.; and Salimans, T. 2022. Classifier-free diffusion guidance. *arXiv preprint arXiv:2207.12598*.
- Karras, T.; Aittala, M.; Aila, T.; and Laine, S. 2022. Elucidating the design space of diffusion-based generative models. *NeurIPS*, 35: 26565–26577.
- Karras, T.; Aittala, M.; Hellsten, J.; Laine, S.; Lehtinen, J.; and Aila, T. 2020. Training generative adversarial networks with limited data. *NeurIPS*, 33: 12104–12114.
- Karras, T.; Laine, S.; and Aila, T. 2019. A style-based generator architecture for generative adversarial networks. In *CVPR*, 4401–4410.
- Kingma, D. P.; and Welling, M. 2014. Auto-encoding variational bayes. *ICLR*.
- Kong, Z.; Ping, W.; Huang, J.; Zhao, K.; and Catanzaro, B. 2021. DiffWave: A Versatile Diffusion Model for Audio Synthesis. In *ICLR*.
- Krizhevsky, A.; Hinton, G.; et al. 2009. Learning multiple layers of features from tiny images.
- Kynkäänniemi, T.; Karras, T.; Laine, S.; Lehtinen, J.; and Aila, T. 2019. Improved precision and recall metric for assessing generative models. *NeurIPS*, 32.
- Li, M.; Qu, T.; Sun, W.; and Moens, M.-F. 2023a. Alleviating Exposure Bias in Diffusion Models through Sampling with Shifted Time Steps. *arXiv preprint arXiv:2305.15583*.
- Li, Y.; Liu, H.; Wu, Q.; Mu, F.; Yang, J.; Gao, J.; Li, C.; and Lee, Y. J. 2023b. Gligen: Open-set grounded text-to-image generation. In *CVPR*, 22511–22521.
- Liu, L.; Ren, Y.; Lin, Z.; and Zhao, Z. 2022. Pseudo Numerical Methods for Diffusion Models on Manifolds. In *ICLR*.
- Liu, Z.; Luo, P.; Wang, X.; and Tang, X. 2015. Deep Learning Face Attributes in the Wild. In *ICCV*.
- Lu, C.; Zhou, Y.; Bao, F.; Chen, J.; Li, C.; and Zhu, J. 2022. Dpm-solver: A fast ode solver for diffusion probabilistic model sampling in around 10 steps. *NeurIPS*, 35: 5775–5787.
- Nichol, A. Q.; and Dhariwal, P. 2021. Improved denoising diffusion probabilistic models. In *ICML*, 8162–8171. PMLR.
- Nichol, A. Q.; Dhariwal, P.; Ramesh, A.; Shyam, P.; Mishkin, P.; Mcgrew, B.; Sutskever, I.; and Chen, M. 2022. GLIDE: Towards Photorealistic Image Generation and Editing with Text-Guided Diffusion Models. In *ICML*, 16784–16804. PMLR.
- Ning, M.; Sangineto, E.; Porrello, A.; Calderara, S.; and Cucchiara, R. 2023. Input Perturbation Reduces Exposure Bias in Diffusion Models. *ICML*.
- Ramesh, A.; Dhariwal, P.; Nichol, A.; Chu, C.; and Chen, M. 2022. Hierarchical Text-Conditional Image Generation with CLIP Latents. *arXiv:2204.06125*.
- Ranzato, M.; Chopra, S.; Auli, M.; and Zaremba, W. 2016. Sequence Level Training with Recurrent Neural Networks. In *ICLR*.
- Rasul, K.; Seward, C.; Schuster, I.; and Vollgraf, R. 2021. Autoregressive denoising diffusion models for multivariate probabilistic time series forecasting. In *ICML*.
- Rombach, R.; Blattmann, A.; Lorenz, D.; Esser, P.; and Ommer, B. 2022. High-resolution image synthesis with latent diffusion models. In *CVPR*, 10684–10695.
- Saharia, C.; Chan, W.; Saxena, S.; Li, L.; Whang, J.; Denton, E. L.; Ghasemipour, K.; Gontijo Lopes, R.; Karagol Ayan, B.; Salimans, T.; et al. 2022. Photorealistic text-to-image diffusion models with deep language understanding. *NeurIPS*, 35: 36479–36494.
- Salimans, T.; and Ho, J. 2022. Progressive Distillation for Fast Sampling of Diffusion Models. In *ICLR*.
- Schmidt, F. 2019. Generalization in Generation: A closer look at Exposure Bias. In *Proceedings of the 3rd Workshop on Neural Generation and Translation@EMNLP-IJCNLP*.
- Sohl-Dickstein, J.; Weiss, E.; Maheswaranathan, N.; and Ganguli, S. 2015. Deep Unsupervised Learning using Nonequilibrium Thermodynamics. In *ICML*.

Song, J.; Meng, C.; and Ermon, S. 2021. Denoising diffusion implicit models. In *ICLR*.

Song, Y.; and Ermon, S. 2019. Generative modeling by estimating gradients of the data distribution. *NeurIPS*, 32.

Song, Y.; Sohl-Dickstein, J.; Kingma, D. P.; Kumar, A.; Ermon, S.; and Poole, B. 2021. Score-Based Generative Modeling through Stochastic Differential Equations. In *ICLR*.

Xiao, Z.; Kreis, K.; and Vahdat, A. 2022. Tackling the Generative Learning Trilemma with Denoising Diffusion GANs. In *ICLR*.

Xu, Y.; Deng, M.; Cheng, X.; Tian, Y.; Liu, Z.; and Jaakkola, T. 2023. Restart Sampling for Improving Generative Processes. *arXiv preprint arXiv:2306.14878*.

Yu, F.; Seff, A.; Zhang, Y.; Song, S.; Funkhouser, T.; and Xiao, J. 2015. Lsun: Construction of a large-scale image dataset using deep learning with humans in the loop. *arXiv preprint arXiv:1506.03365*.

Zhang, L.; and Agrawala, M. 2023. Adding conditional control to text-to-image diffusion models. *arXiv preprint arXiv:2302.05543*.

Zhao, W.; Bai, L.; Rao, Y.; Zhou, J.; and Lu, J. 2023. UniPC: A Unified Predictor-Corrector Framework for Fast Sampling of Diffusion Models. *arXiv preprint arXiv:2302.04867*.

Zheng, G.; Zhou, X.; Li, X.; Qi, Z.; Shan, Y.; and Li, X. 2023. LayoutDiffusion: Controllable Diffusion Model for Layout-to-image Generation. In *CVPR*, 22490–22499.

Zhou, L.; Du, Y.; and Wu, J. 2021. 3d shape generation and completion through point-voxel diffusion. In *ICCV*, 5826–5835.

Appendices

Derivation of $q(\hat{\mathbf{x}}_t | \mathbf{x}_{t+1}, \mathbf{x}_\theta^{t+1})$

We show the full derivation of Eq. 8 below. From Eq. 23 to Eq. 24, we plug in $\mathbf{x}_\theta^{t+1} = \mathbf{x}_0 + e_{t+1}\boldsymbol{\epsilon}_0$ (Eq. 15) and $\mathbf{x}_{t+1} = \sqrt{\bar{\alpha}_{t+1}}\mathbf{x}_0 + \sqrt{1 - \bar{\alpha}_{t+1}}\boldsymbol{\epsilon}$ (Eq. 4)

$$\begin{aligned} \hat{\mathbf{x}}_t &= \mu_\theta(\mathbf{x}_{t+1}, t+1) + \sqrt{\tilde{\beta}_{t+1}}\boldsymbol{\epsilon}_1 \\ &= \frac{\sqrt{\bar{\alpha}_t}\beta_{t+1}}{1 - \bar{\alpha}_{t+1}}\mathbf{x}_\theta^{t+1} + \frac{\sqrt{\bar{\alpha}_{t+1}}(1 - \bar{\alpha}_t)}{1 - \bar{\alpha}_{t+1}}\mathbf{x}_{t+1} + \sqrt{\tilde{\beta}_{t+1}}\boldsymbol{\epsilon}_1 \end{aligned} \quad (23)$$

$$= \frac{\sqrt{\bar{\alpha}_t}\beta_{t+1}}{1 - \bar{\alpha}_{t+1}}(\mathbf{x}_0 + e_{t+1}\boldsymbol{\epsilon}_0) + \frac{\sqrt{\bar{\alpha}_{t+1}}(1 - \bar{\alpha}_t)}{1 - \bar{\alpha}_{t+1}}(\sqrt{\bar{\alpha}_{t+1}}\mathbf{x}_0 + \sqrt{1 - \bar{\alpha}_{t+1}}\boldsymbol{\epsilon}) + \sqrt{\tilde{\beta}_{t+1}}\boldsymbol{\epsilon}_1 \quad (24)$$

$$= \frac{\sqrt{\bar{\alpha}_t}\beta_{t+1}}{1 - \bar{\alpha}_{t+1}}\mathbf{x}_0 + \frac{\sqrt{\bar{\alpha}_{t+1}}(1 - \bar{\alpha}_t)}{1 - \bar{\alpha}_{t+1}}\sqrt{\bar{\alpha}_{t+1}}\mathbf{x}_0 + \frac{\sqrt{\bar{\alpha}_t}\beta_{t+1}}{1 - \bar{\alpha}_{t+1}}e_{t+1}\boldsymbol{\epsilon}_0 + \frac{\sqrt{\bar{\alpha}_{t+1}}(1 - \bar{\alpha}_t)}{1 - \bar{\alpha}_{t+1}}\sqrt{1 - \bar{\alpha}_{t+1}}\boldsymbol{\epsilon} + \sqrt{\tilde{\beta}_{t+1}}\boldsymbol{\epsilon}_1 \quad (25)$$

$$= \frac{\sqrt{\bar{\alpha}_t}\beta_{t+1} + \sqrt{\bar{\alpha}_{t+1}}(1 - \bar{\alpha}_t)\sqrt{\bar{\alpha}_{t+1}}}{1 - \bar{\alpha}_{t+1}}\mathbf{x}_0 + \frac{\sqrt{\bar{\alpha}_t}\beta_{t+1}}{1 - \bar{\alpha}_{t+1}}e_{t+1}\boldsymbol{\epsilon}_0 + \frac{\sqrt{\bar{\alpha}_{t+1}}(1 - \bar{\alpha}_t)}{1 - \bar{\alpha}_{t+1}}\sqrt{1 - \bar{\alpha}_{t+1}}\boldsymbol{\epsilon} + \sqrt{\tilde{\beta}_{t+1}}\boldsymbol{\epsilon}_1 \quad (26)$$

$$= \frac{\sqrt{\bar{\alpha}_t}(1 - \alpha_{t+1}) + \sqrt{\bar{\alpha}_{t+1}}(1 - \bar{\alpha}_t)\sqrt{\bar{\alpha}_{t+1}}}{1 - \bar{\alpha}_{t+1}}\mathbf{x}_0 + \frac{\sqrt{\bar{\alpha}_t}\beta_{t+1}}{1 - \bar{\alpha}_{t+1}}e_{t+1}\boldsymbol{\epsilon}_0 + \frac{\sqrt{\bar{\alpha}_{t+1}}(1 - \bar{\alpha}_t)}{1 - \bar{\alpha}_{t+1}}\sqrt{1 - \bar{\alpha}_{t+1}}\boldsymbol{\epsilon} + \sqrt{\tilde{\beta}_{t+1}}\boldsymbol{\epsilon}_1 \quad (27)$$

$$= \frac{\sqrt{\bar{\alpha}_t}(1 - \alpha_{t+1}) + \alpha_{t+1}(1 - \bar{\alpha}_t)\sqrt{\bar{\alpha}_t}}{1 - \bar{\alpha}_{t+1}}\mathbf{x}_0 + \frac{\sqrt{\bar{\alpha}_t}\beta_{t+1}}{1 - \bar{\alpha}_{t+1}}e_{t+1}\boldsymbol{\epsilon}_0 + \frac{\sqrt{\bar{\alpha}_{t+1}}(1 - \bar{\alpha}_t)}{1 - \bar{\alpha}_{t+1}}\sqrt{1 - \bar{\alpha}_{t+1}}\boldsymbol{\epsilon} + \sqrt{\tilde{\beta}_{t+1}}\boldsymbol{\epsilon}_1 \quad (28)$$

$$= \frac{\sqrt{\bar{\alpha}_t}(1 - \alpha_{t+1} + \alpha_{t+1} - \bar{\alpha}_{t+1})}{1 - \bar{\alpha}_{t+1}}\mathbf{x}_0 + \frac{\sqrt{\bar{\alpha}_t}\beta_{t+1}}{1 - \bar{\alpha}_{t+1}}e_{t+1}\boldsymbol{\epsilon}_0 + \frac{\sqrt{\bar{\alpha}_{t+1}}(1 - \bar{\alpha}_t)}{1 - \bar{\alpha}_{t+1}}\sqrt{1 - \bar{\alpha}_{t+1}}\boldsymbol{\epsilon} + \sqrt{\tilde{\beta}_{t+1}}\boldsymbol{\epsilon}_1 \quad (29)$$

$$= \sqrt{\bar{\alpha}_t}\mathbf{x}_0 + \frac{\sqrt{\bar{\alpha}_t}\beta_{t+1}}{1 - \bar{\alpha}_{t+1}}e_{t+1}\boldsymbol{\epsilon}_0 + \frac{\sqrt{\bar{\alpha}_{t+1}}(1 - \bar{\alpha}_t)}{1 - \bar{\alpha}_{t+1}}\sqrt{1 - \bar{\alpha}_{t+1}}\boldsymbol{\epsilon} + \sqrt{\tilde{\beta}_{t+1}}\boldsymbol{\epsilon}_1 \quad (30)$$

From Eq. 30, we know that the mean of $q(\hat{\mathbf{x}}_t | \mathbf{x}_{t+1}, \mathbf{x}_\theta^{t+1})$ is $\sqrt{\bar{\alpha}_t}\mathbf{x}_0$. We now focus on the variance by looking at $\frac{\sqrt{\bar{\alpha}_t}\beta_{t+1}}{1 - \bar{\alpha}_{t+1}}e_{t+1}\boldsymbol{\epsilon}_0 + \frac{\sqrt{\bar{\alpha}_{t+1}}(1 - \bar{\alpha}_t)}{1 - \bar{\alpha}_{t+1}}\sqrt{1 - \bar{\alpha}_{t+1}}\boldsymbol{\epsilon} + \sqrt{\tilde{\beta}_{t+1}}\boldsymbol{\epsilon}_1$:

$$\text{Var}(\hat{\mathbf{x}}_t) = \left(\frac{\sqrt{\bar{\alpha}_t}\beta_{t+1}}{1 - \bar{\alpha}_{t+1}}e_{t+1}\right)^2 + \left(\frac{\sqrt{\bar{\alpha}_{t+1}}(1 - \bar{\alpha}_t)}{1 - \bar{\alpha}_{t+1}}\sqrt{1 - \bar{\alpha}_{t+1}}\right)^2 + \tilde{\beta}_{t+1} \quad (31)$$

$$= \left(\frac{\sqrt{\bar{\alpha}_t}\beta_{t+1}}{1 - \bar{\alpha}_{t+1}}e_{t+1}\right)^2 + \left(\frac{\sqrt{\bar{\alpha}_{t+1}}(1 - \bar{\alpha}_t)}{1 - \bar{\alpha}_{t+1}}\sqrt{1 - \bar{\alpha}_{t+1}}\right)^2 + \frac{(1 - \bar{\alpha}_t)(1 - \alpha_{t+1})}{1 - \bar{\alpha}_{t+1}} \quad (32)$$

$$= \left(\frac{\sqrt{\bar{\alpha}_t}\beta_{t+1}}{1 - \bar{\alpha}_{t+1}}e_{t+1}\right)^2 + \frac{\alpha_{t+1}(1 - \bar{\alpha}_t)^2}{1 - \bar{\alpha}_{t+1}} + \frac{(1 - \bar{\alpha}_t)(1 - \alpha_{t+1})}{1 - \bar{\alpha}_{t+1}} \quad (33)$$

$$= \left(\frac{\sqrt{\bar{\alpha}_t}\beta_{t+1}}{1 - \bar{\alpha}_{t+1}}e_{t+1}\right)^2 + \frac{\alpha_{t+1}(1 - \bar{\alpha}_t)^2 + (1 - \bar{\alpha}_t)(1 - \alpha_{t+1})}{1 - \bar{\alpha}_{t+1}} \quad (34)$$

$$= \left(\frac{\sqrt{\bar{\alpha}_t}\beta_{t+1}}{1 - \bar{\alpha}_{t+1}}e_{t+1}\right)^2 + \frac{(1 - \bar{\alpha}_t)[\alpha_{t+1}(1 - \bar{\alpha}_t) + (1 - \alpha_{t+1})]}{1 - \bar{\alpha}_{t+1}} \quad (35)$$

$$= \left(\frac{\sqrt{\bar{\alpha}_t}\beta_{t+1}}{1 - \bar{\alpha}_{t+1}}e_{t+1}\right)^2 + \frac{(1 - \bar{\alpha}_t)[\alpha_{t+1} - \bar{\alpha}_{t+1} + 1 - \alpha_{t+1}]}{1 - \bar{\alpha}_{t+1}} \quad (36)$$

$$= \left(\frac{\sqrt{\bar{\alpha}_t}\beta_{t+1}}{1 - \bar{\alpha}_{t+1}}e_{t+1}\right)^2 + \frac{(1 - \bar{\alpha}_t)[1 - \bar{\alpha}_{t+1}]}{1 - \bar{\alpha}_{t+1}} \quad (37)$$

$$= \left(\frac{\sqrt{\bar{\alpha}_t}\beta_{t+1}}{1 - \bar{\alpha}_{t+1}}e_{t+1}\right)^2 + 1 - \bar{\alpha}_t \quad (38)$$

$$(39)$$

Practical Variance Error of Sampling Distribution $q(\hat{\mathbf{x}}_t | \mathbf{x}_{t+1}, \mathbf{x}_\theta^{t+1})$

We measure the variance error of sampling distribution $q(\hat{\mathbf{x}}_t | \mathbf{x}_{t+1}, \mathbf{x}_\theta^{t+1})$ under single-step and multi-step reverse diffusion using Algorithm 2 and Algorithm 3, respectively. Note that, the multi-step variance error measurement is actually the same

as the exposure bias δ_t evaluation and we denote the single-step variance error as Δ_t . The experiments are implemented on CIFAR-10 (Krizhevsky, Hinton et al. 2009) dataset and ADM model (Dhariwal and Nichol 2021). The key difference between Δ_t and δ_t measurement is that the former can get access to the ground truth input \mathbf{x}_t at each sampling step t , while the latter is only exposed to the predicted $\hat{\mathbf{x}}_t$ in the iterative sampling process.

Algorithm 2: Variance error under single-step sampling

```

1: Initialize  $\Delta_t = 0, n_t = list()$  ( $\forall t \in \{1, \dots, T - 1\}$ )
2: for  $t := T, \dots, 1$  do
3:   repeat
4:      $\mathbf{x}_0 \sim q(\mathbf{x}_0), \boldsymbol{\epsilon} \sim \mathcal{N}(\mathbf{0}, \mathbf{I})$ 
5:      $\mathbf{x}_t = \sqrt{\bar{\alpha}_t} \mathbf{x}_0 + \sqrt{1 - \bar{\alpha}_t} \boldsymbol{\epsilon}$ 
6:      $\hat{\mathbf{x}}_{t-1} = \frac{1}{\sqrt{\alpha_t}} (\mathbf{x}_t - \frac{\beta_t}{\sqrt{1-\alpha_t}} \boldsymbol{\epsilon}_\theta(\mathbf{x}_t, t)) + \sqrt{\tilde{\beta}_t} \mathbf{z}$  ( $\mathbf{z} \sim \mathcal{N}(\mathbf{0}, \mathbf{I})$ )
7:      $n_{t-1}.append(\hat{\mathbf{x}}_{t-1} - \sqrt{\bar{\alpha}_{t-1}} \mathbf{x}_0)$ 
8:   until 50k iterations
9: end for
10: for  $t := T, \dots, 1$  do
11:    $\hat{\beta}_t = \text{numpy.var}(n_t)$ 
12:    $\Delta_t = \hat{\beta}_t - \bar{\beta}_t$ 
13: end for

```

Algorithm 3: Variance error under multi-step sampling

```

1: Initialize  $\delta_t = 0, n_t = list()$  ( $\forall t \in \{1, \dots, T - 1\}$ )
2: repeat
3:    $\mathbf{x}_0 \sim q(\mathbf{x}_0), \boldsymbol{\epsilon} \sim \mathcal{N}(\mathbf{0}, \mathbf{I})$ 
4:    $\mathbf{x}_T = \sqrt{\bar{\alpha}_T} \mathbf{x}_0 + \sqrt{1 - \bar{\alpha}_T} \boldsymbol{\epsilon}$ 
5:   for  $t := T, \dots, 1$  do
6:     if  $t == T$  then  $\hat{\mathbf{x}}_t = \mathbf{x}_T$ 
7:      $\hat{\mathbf{x}}_{t-1} = \frac{1}{\sqrt{\alpha_t}} (\hat{\mathbf{x}}_t - \frac{\beta_t}{\sqrt{1-\alpha_t}} \boldsymbol{\epsilon}_\theta(\hat{\mathbf{x}}_t, t)) + \sqrt{\tilde{\beta}_t} \mathbf{z}$  ( $\mathbf{z} \sim \mathcal{N}(\mathbf{0}, \mathbf{I})$ )
8:      $n_{t-1}.append(\hat{\mathbf{x}}_{t-1} - \sqrt{\bar{\alpha}_{t-1}} \mathbf{x}_0)$ 
9:   end for
10: until 50k iterations
11: for  $t := T, \dots, 1$  do
12:    $\hat{\beta}_t = \text{numpy.var}(n_t)$ 
13:    $\delta_t = \hat{\beta}_t - \bar{\beta}_t$ 
14: end for

```

Recall and Precision Results

Our method Epsilon Scaling does not affect the recall and precision of the base model. We present the complete recall and precision (Kynkäänniemi et al. 2019) results in Table 5 using the code provided by ADM (Dhariwal and Nichol 2021). ADM-ES achieve higher recalls and slightly lower previsions across the five datasets. But the overall differences are minor.

Table 5: Recall and precision of ADM and ADM-ES using 100-step sampling.

Model	CIFAR-10 32×32		LSUN tower 64×64		FFHQ 128×128		ImageNet 64×64		ImageNet 128×128	
	recall	precision	recall	precision	recall	precision	recall	precision	recall	precision
ADM	0.591	0.691	0.605	0.645	0.497	0.696	0.621	0.738	0.586	0.771
ADM-ES	0.613	0.684	0.606	0.641	0.545	0.683	0.632	0.726	0.592	0.771

Epsilon Scaling Parameters: k, b

We present the parameters k, b of Epsilon Scaling we used in all of our experiments in Table 6 and Table 7 for reproducibility. Apart from that, we provide guidance on how to search for the optimal parameters even though they are dependent on the dataset and how well the base model is trained. Our suggestions are:

- First search for the optimal uniform schedule λ_t (i.e. $\lambda_t = b$) with a large stride, for example, $b = 1.001, 1.003, 1.005 \dots$
- After locating the coarse range of the optimal b , apply a smaller stride to finetune the initial b .
- In general, the optimal b will decrease as the number of sampling steps T' increases.
- If one is interested in finding the optimal linear schedule $\lambda_t = kt + b$, we suggest taking the optimal uniform schedule $\lambda_t = b$ as the baseline and maintaining the mean of $\lambda_t = kt + b$ equal to the baseline. Then, a small k (for example, 0.0001) is a good starting point.
- Instead of generating 50k samples for FID computation, we find that 10k samples are enough for parameter searching.

Table 6: Parameters k and b of Epsilon Scaling schedule $\lambda_t = kt + b$ we used on ADM baseline. We remain the FID results in the table for comparisons and remark k, b underneath FIDs

T'	Model	Unconditional			Conditional	
		CIFAR-10 32×32	LSUN tower 64×64	FFHQ 128×128	ImageNet 64×64	ImageNet 128×128
100	ADM	3.37	3.59	14.52	2.71	3.55
	ADM-ES	2.17 (b=1.017)	2.91 (b=1.006)	6.77 (b=1.005)	2.39 (b=1.006)	3.37 (b=1.004)
50	ADM	4.43	7.28	26.15	3.75	5.15
	ADM-ES	2.49 (b=1.017)	3.68 (b=1.007)	9.50 (b=1.007)	3.07 (b=1.006)	4.33 (b=1.004)
20	ADM	10.36	23.92	59.35	10.96	12.48
	ADM-ES	5.15 (b=1.017)	8.22 (b=1.011)	26.14 (b=1.008)	7.52 (b=1.006)	9.95 (b=1.005)
	ADM-ES*	4.31 (k=0.0025, b=1.0)	7.60 (k=0.0008, b=1.0034)	24.83 (k=0.0004, b=1.0042)	7.37 (k=0.0002, b=1.0041)	9.86 (k=0.00022, b=1.00291)

Table 7: Parameter b of Epsilon Scaling schedule $\lambda_t = kt + b, (k = 0)$ we used on DDIM/DDPM and LDM baseline. We remain the FID results in the table for comparisons and remark b underneath FIDs

T'	Model	CIFAR-10 32×32		CelebA 64×64		T'	Model	FFHQ 256×256	CelebA-HQ 256×256
		$\eta = 0$	$\eta = 1$	$\eta = 0$	$\eta = 1$				
100	DDIM	4.06	6.73	5.67	11.33	100	LDM	10.90	9.31
	DDIM-ES	3.38 (b=1.0014)	4.01 (b=1.03)	5.05 (b=1.003)	4.45 (b=1.04)		LDM-ES	9.83 (b=1.00015)	7.36 (b=1.0009)
50	DDIM	4.82	10.29	6.88	15.09	50	LDM	14.34	13.95
	DDIM-ES	4.17 (b=1.0030)	4.57 (b=1.04)	6.20 (b=1.004)	5.57 (b=1.05)		LDM-ES	11.57 (b=1.0016)	9.16 (b=1.003)
20	DDIM	8.21	20.15	10.43	22.61	20	LDM	33.13	29.62
	DDIM-ES	6.54 (b=1.0052)	7.78 (b=1.05)	10.38 (b=1.001)	11.83 (b=1.06)		LDM-ES	20.91 (b=1.007)	15.68 (b=1.010)

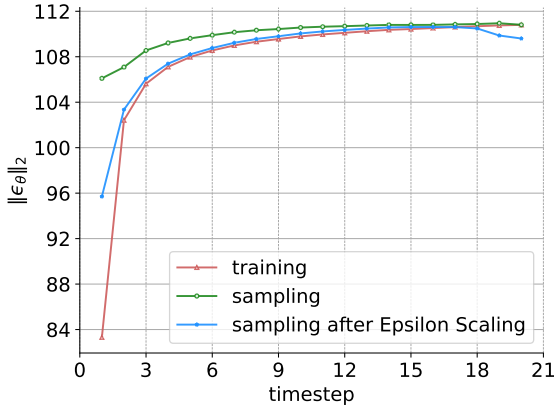
Epsilon Scaling Alleviates Exposure Bias

In Section , we have explicitly shown that Epsilon Scaling reduces the exposure bias of diffusion models via refining the sampling trajectory and achieves a lower δ_t on CIFAR-10 dataset.

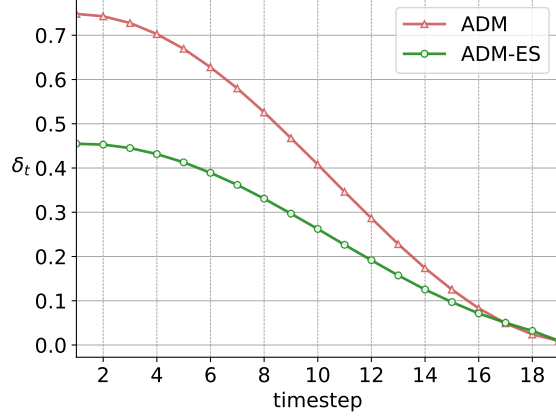
We now replicate these experiments on other datasets using the same base model ADM and 20-step sampling. Figure 7 and Figure 8 display the corresponding results on LSUN tower 64×64 and FFHQ 128×128 datasets. Similar to the phenomenon on CIFAR-10, Epsilon Scaling consistently obtains a smaller exposure bias δ_t and pushes the sampling trajectory to the vector field learned in the training stage.

Qualitative Comparison

In Section , we have presented the sample quality comparison between the base model sampling and Epsilon Scaling sampling on FFHQ 128×128 dataset. Applying the same experimental settings, we show more qualitative contrasts between ADM and ADM-ES on the dataset CIFAR-10 32×32 (Figure 9), LSUN tower 64×64 (Figure 10), ImageNet 64×64 (Figure 11) and ImageNet 128×128 (Figure 12). Also, we provide the qualitative comparison between LDM and LDM-ES on the dataset CelebA-HQ 256×256 (Figure 13). These sample comparisons clearly state that Epsilon Scaling effectively improves the sample quality from various perspectives, including illumination, colour, object coherence, background details and so on.

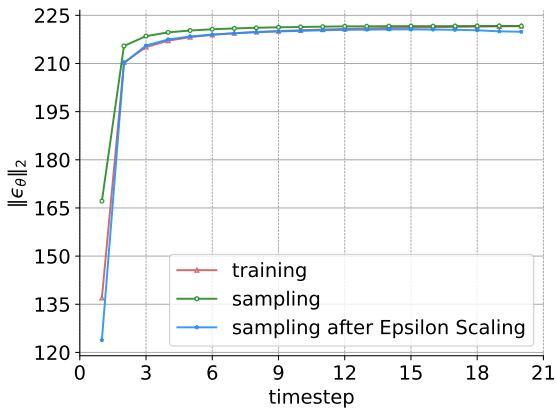


(a) L2-norm of $\epsilon_{\theta}(\cdot)$ on LSUN tower 64×64

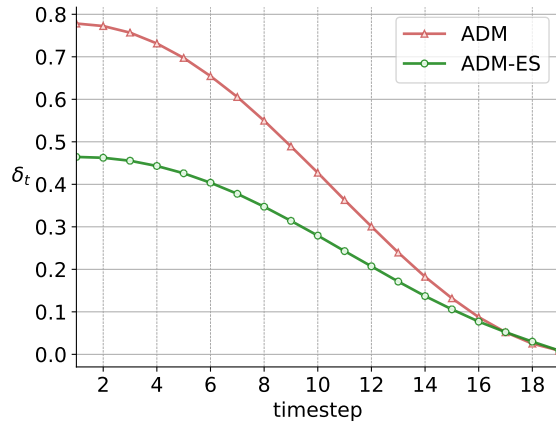


(b) Exposure bias measured by δ_t on LSUN tower 64×64

Figure 7: Left: after applying Epsilon Scaling, the sampling $\|\epsilon_{\theta}\|_2$ (blue) gets closer to the training $\|\epsilon_{\theta}\|_2$ (red). Right: Epsilon Scaling achieves a smaller δ_t at the end of sampling ($t = 1$)



(a) L2-norm of $\epsilon_{\theta}(\cdot)$ on FFHQ 128×128



(b) Exposure bias measured by δ_t on FFHQ 128×128

Figure 8: Left: after applying Epsilon Scaling, the sampling $\|\epsilon_{\theta}\|_2$ (blue) gets closer to the training $\|\epsilon_{\theta}\|_2$ (red). Right: Epsilon Scaling achieves a smaller δ_t at the end of sampling ($t = 1$).

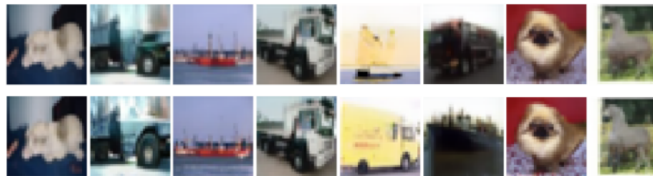


Figure 9: Qualitative comparison between ADM (first row) and ADM-ES (second row) on CIFAR-10 32×32

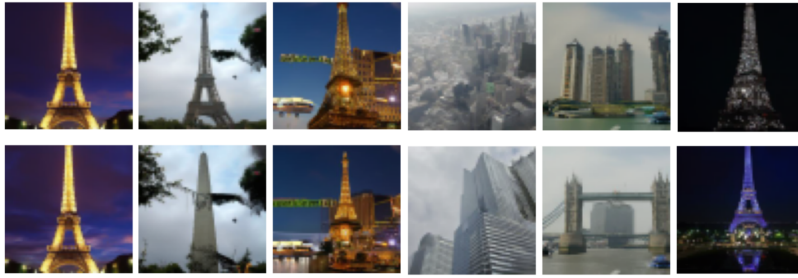


Figure 10: Qualitative comparison between ADM (first row) and ADM-ES (second row) on LSUN tower 64×64



Figure 11: Qualitative comparison between ADM (first row) and ADM-ES (second row) on ImageNet 64×64



Figure 12: Qualitative comparison between ADM (first row) and ADM-ES (second row) on ImageNet 128×128



Figure 13: Qualitative comparison between LDM (first row) and LDM-ES (second row) on CelebA-HQ 256×256